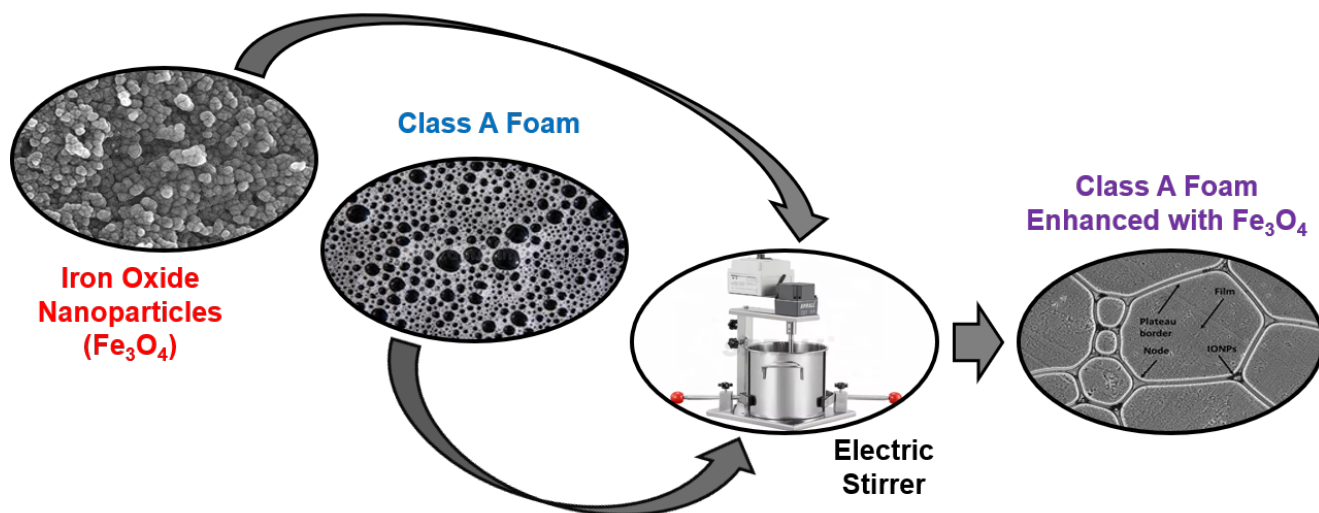# Graphical Abstract

Investigating the impact of iron oxide nanoparticles on the stability of class A foam for wildfire suppression

Ioannis Papagiannis,Mauro S. Innocente,Joshua D. Davies,Joshua L. Ryan,Evangelos I. Gkanas

Highlights

Investigating the impact of iron oxide nanoparticles on the stability of class A foam for wildfire suppression

Ioannis Papagiannis,Mauro S. Innocente,Joshua D. Davies,Joshua L. Ryan,Evangelos I. Gkanas

- Iron Oxide Nanoparticles (IONPs) improve foam stability by altering bubble structure.

- IONPs also improve foam stability by altering surface tension.

- Reflux is more cost-effective and practical than hydrothermal synthesis in the lab.

- X-Ray Diffraction (XRD) analysis confirms crystalline structure of synthesised IONPs.

- A crystalline structure is indicative of their potential to enhance foam stability.

Investigating the impact of iron oxide nanoparticles on the stability of class A foam for wildfire suppression

Ioannis Papagiannis[a,*], Mauro S. Innocente[a,*], Joshua D. Davies[b], Joshua L. Ryan[b] and Evangelos I. Gkanas[a,*]

[a]*Autonomous Vehicles & Artificial Intelligence Laboratory, Coventry University, 7th Floor Friars House, Manor House Drive, Coventry, CV1 2TE, UK*
[b]*Department of Chemistry, University of Warwick, Coventry, CV4 7SH, UK*

ARTICLE INFO

Keywords:
Firefighting foams
Foam stability
Bubble morphology
Surface tension
Synthesis

ABSTRACT

This study investigates the effect of Iron Oxide Nanoparticles (IONPs) on the stability of a class A foam. IONPs are synthesised via two different pathways, namely the *reflux* and the *hydrothermal* methods. The synthesised nanoparticles are then added to the foam solution at different concentrations, applying various techniques to test how they affect properties and processes such as particle size distribution, surface tension, and coalescence. Results show that (*i*) the addition of IONPs improves the foam stability by reducing the bubble coarsening and disproportionation; (*ii*) the IONPs assemble at the plateau borders and nodes of the bubbles creating a protective layer on the gas–liquid interface, which delays foam drainage hence improving foam stability; and (*iii*) stability is also improved by the increase in the foam half-life due to the accumulation of nanoparticles on the surface of the bubble. IONPs obtained using the reflux method are shown to affect the firefighting foam more positively.

1. Introduction

Aqueous foams, also known as wet foams, undergo rapid changes due to gravity drainage, which leads to the collapse of their structure over time due to inherent low stability [1, 2, 3, 4]. This behavior is attributed to the Laplace pressure difference facilitating the slow diffusion of gas through the bubble walls and causing smaller bubbles to shrink more rapidly until they eventually disappear [5]. These foams are utilised in a variety of applications, including mineral flotation, the food industry, firefighting, and personal care products [1, 3, 6, 7]. More specifically, aqueous foam can be defined as a dispersion system where the dispersing agent is gas (i.e. air) and the dispersive environment is liquid [8]. In the last decade, there has been a growing interest in stabilising the foams [9]. Firefighting foams face challenges related to their instability, which can compromise their efficiency in fire suppression. Advancements in nanotechnology offer a potential route to enhancing foam stability, with nanoparticles accumulating at the gas–liquid interface forming a dense wrap, thus delaying foam drainage and preventing gas diffusion between bubbles [10, 11].

Water does not produce foam without the addition of surfactants. One of their crucial effects is that they adsorb at the interfaces of the liquid, reducing foam drainage by preventing bubble coalescence through steric effects [12]. Foam drainage refers to the separation between the gas and the liquid phases, which is achieved by the downward liquid flow away from the foam due to differences in density [13]. During drainage, several types of deformation processes may occur. The liquid flowing downwards due to gravity from the top of the bubble droplet would be initially subjected to dilatation forces, whilst it would be compressed upon reaching the bottom [14]. The longer the foam drainage time and half-life of the foam, the more slowly the foam decays. This means better foam stability. Foam half-life is defined as the time required for the initial foam volume to be reduced by half [15]. High-stability foams can resist bubble coalescence and collapse, resulting in a longer foam half-life.

Nanoparticles (NPs) are known to be great additives to enhance some properties of other materials [16, 17, 18]. Solid NPs behave differently in thin films than in bulk, and they can have a significant effect in the stability of the foam films. In this work, they alter the mechanical properties of the foam by reducing both drainage and coarsening [19].

The stabilisation of firefighting foams by adding NPs was investigated by Yang et al. [20], who argue that the role that SiO_2 NPs play in the stability of the foam depends on their concentration. At lower concentrations, they appear to reduce the electrostatic energy without forming a network, leading to decreased foam stability. Conversely, they significantly enhance foam stability at higher concentrations, seemingly by creating a blocking layer in the plateau borders. Yekeen et al. [21] suggest that the main mechanisms for SiO_2 NPs to increase foam stability is their adsorption and aggregation at the foam lamellae, increasing film thickness and dilational viscoelasticity. The NPs adsorbed at the interface impede the bubble coalescence and form an interfacial protective layer that hinders the gas diffusion outward of the bubble. Tang et al. [22] added SiO_2 NPs into an alcohol-resistant foam and found that foam stability was increased by decreasing the size of the NPs to 15 nm. This is because the drainage process is influenced by weight, with heavier particles leading to faster drainage as they pull the liquid more strongly towards the bottom of the foam structure. The aggregation of NPs at the gas-liquid interface plays an

*Corresponding author

✉ papagiai@uni.coventry.ac.uk (I. Papagiannis);
Mauro.S.Innocente@coventry.ac.uk (M.S. Innocente);
ac1029@coventry.ac.uk (E.I. Gkanas)

🌐 availab.org (M.S. Innocente)

ORCID(s): 0000-0002-9648-6724 (I. Papagiannis); 0000-0001-8836-2839 (M.S. Innocente); 0000-0003-0934-7564 (E.I. Gkanas)

important role in stabilising the aqueous solution by preventing droplets from coalescing. The adsorption of NPs on the interface is irreversible, which implies that they are difficult to detach, providing solid properties to the bubble interface [21, 23, 24]. Generally, a lower particle size indicates that NPs may easily collect sufficient oxygen to combust [25].

Iron oxide nanoparticles (IONPs) have gained significant attention in recent years due to their flame retardancy and smoke suppression properties [26, 27, 28, 29]. In addition, they are known for their low toxicity and bio-compatibility [30]. The controlled synthesis of IONPs with tailored size and structural properties may influence the stability and effectiveness of firefighting foams [31]. Given their flame retardancy properties (with melting temperature higher than 1,500 °C), IONPs may be added to aqueous systems to improve their thermal stability. Furthermore, it has been shown that iron oxide could adsorb small organic molecules subsequently catalysing them into chars, thus improving the thermal stability of a flame retardant at higher temperatures [26]. The small organic molecules are adsorbed in the iron oxide forming aromatic cyclic structures that are chars through the catalysis of Fe^{3+} ions. Kong et al. [32] demonstrated that iron has a significant impact on radical trapping and increases the onset temperature of thermal degradation in nano-composites. The iron could act as an antioxidant and radical trap, thus improving the thermal stability of the nano-composites. IONPs show a good potential synergistic effect in improving the thermal stability of foams as they have desirable properties such as catalysis and capture of radicals [26, 33]. In general, liquid-based agents reduce the number of radicals released and slow the spread of fire [34, 35]. The flammability of certain materials is highly dependent on radical concentration [36], with radical trapping effectively eliminating the ability of the material to burn [34].

This research investigates the impact of adding IONPs on the stability of a commercial class A foam. The NPs are synthesised via the *hydrothermal* and the *reflux* methods aiming to explore potential synergistic effects that enhance wildfire suppression capabilities. The focus is on the drainage rate and bubble surface morphology of the foam. Tests are conducted to evaluate the influence of different concentrations of IONPs on the stability of the foam, while zeta potential, surface tension, and foam drainage changes are examined to elucidate the IONPs stabilisation mechanism. The remainder of this paper is organised as follows: the experimental details are provided in Section 2, including materials, NPs synthesis and characterisation, and foam preparation; Section 3 presents the results obtained and provides a detailed discussion of the findings; Section 4 identifies the interaction mechanisms between IONPs and class A foams; whilst Section 5 offers some conclusions.

2. Experimental details

2.1. Materials

Iron(II) chloride tetrahydrate ($FeCl_2 \cdot 4\,H_2O$) and ammonium hydroxide solution (28 % NH_3) were purchased from Thermo Fisher Scientific. Forexpan firefighting class A foam concentrate 0.1–1 % was purchased from Angus Fire UK. Triple Distilled (3D) water is used. All materials are used without any further purification.

2.2. Solvothermal synthesis of IONPs

IONPs are synthesised by means of a one-step solvothermal process. An amount of 4.3 g of $FeCl_2 \cdot 4\,H_2O$; 50 mL of distilled (3D) water; and 10 mL of ammonium hydroxide solution (NH_4OH) are used for the synthesis. Initially, the $FeCl_2 \cdot 4\,H_2O$ is dispersed into 3D water to form a homogeneous solution, and then the NH_4OH is added dropwise under vigorous stirring. The final solution is ultrasonically mixed for an additional 30 min. The obtained solution is transferred to a 60 mL Teflon-lined autoclave and sealed. The autoclave is placed in a preheated oven at 135 °C for three hours. Then, temperature decreases naturally. The resulting material is separated from the solvent by centrifugation and successively washed with ultra-pure water at 4, 200 rpm at least three times, and then dried overnight in a vacuum at 65 °C. This material is named H-Fe_3O_4.

2.3. Reflux synthesis of IONPs

The precursors with the same stoichiometry described in Section 2.2 are used here. The reaction takes place in a 500 mL three-neck flask placed in a heating mantle. The three-neck flask is connected to a reflux condenser system open to the atmosphere. After being heated for one hour at 100 °C, the solution is let to cool down at room temperature. It is then transferred for centrifugation and successively washed with ultra-pure water at 4,200 rpm at least three times, and then dried overnight in a vacuum at 65 °C. This material is named R-Fe_3O_4.

2.4. Preparation of the foam solution

For the foam drainage experiments, a $100 - ml$ mixed solution of conventional class A foam concentrate, triple-distilled water, and IONPs is prepared. The foam solution consists of 0.6 % (v/v) foam concentrate and 99.4 mL of deionised water, as per manufacturer recommendation [37]. Various concentrations of IONPs are added to the foam solution, namely 0 wt%, 0.025 wt%, 0.05 wt%, and 0.1 wt%. The foam solution is mixed using an overhead stirrer. The foam dispersions prepared and tested are listed in Table 1.

2.5. Foam generation

The foam is generated using two syringes connected with a tube [3] as in Fig. 1. For all experiments, the volumes of gas (air) and liquid (foam solution) are 40 mL and 20 mL, respectively. Foam is created by pushing the liquid and gas dispersion repeatedly over 15 times.

### 2.6. Characterisation of the IONPs

X-ray diffraction (XRD) analysis is performed using a D8 Advanced DaVinci system (Bruker) equipped with a lynx eye detector. Diffraction patterns are detected using Cu-$K\alpha$ radiation of 1.54 Å wavelength, and the 2θ scan is performed from 20° to 90°. A step size of 0.0102° and a time-step

Table 1
Details of the prepared foam solutions.

Sample Name	IONPs Preparation Method	Class A Foam Concentrate (%)	Triple Distilled Water (mL)	IONPs Concentration (wt%)
Plain Foam	Hydrothermal	0.6	99.4	0
H-1	Hydrothermal	0.6	99.4	0.025
H-2	Hydrothermal	0.6	99.4	0.05
H-3	Hydrothermal	0.6	99.4	0.1
Plain Foam	Reflux	0.6	99.4	0
R-1	Reflux	0.6	99.4	0.025
R-2	Reflux	0.6	99.4	0.05
R-3	Reflux	0.6	99.4	0.1
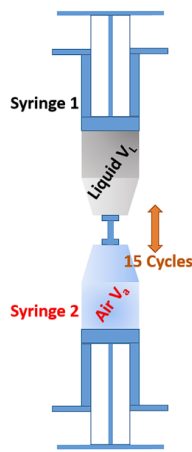
Figure 1: Foam generation via double syringe technique.

of 0.12 s are used during the scanning process. The Scanning Electron Microscopy (SEM) micrographs are recorded with a ZEISS Gemini SEM 360 microscope. The Fourier Transform Infrared (FTIR) spectra are recorded with the Thermo Scientific Nicolet 50 FTIR spectrometer. The foam morphology is studied using a Nikon digital microscope.

Dynamic light scattering (DLS) is used to monitor the change in hydrodynamic radius (particle size) and aggregates in the solution. Measurements are carried out on a Litesizer™ 500 instrument, which uses a laser to illuminate the particles, and the scattered light is detected and analysed to determine their size distribution.

Drop shape analysis (DSA) is used to measure the surface tension using a Drop Shape Analyser DSA 100. This instrument allows for precise and accurate measurements of the surface tension of liquids using the pendant drop method.

3. Results and discussion

3.1. X-Ray diffraction

The crystal structures of the synthesised R-Fe$_3$O$_4$ and H-Fe$_3$O$_4$ IONPs are characterised using X-Ray Diffraction

(XRD). The XRD spectra of both materials are presented in Fig. 2 (a), where various diffraction peaks appear due to the crystalline nature of the samples. In the XRD analysis of the IONPs, it can be observed that the dominant phase present in the sample is magnetite (Fe$_3$O$_4$), as evidenced by the characteristic diffraction peaks. However, a closer examination of the XRD pattern reveals the presence of an additional phase identified as goethite (α-FeOOH), as shown in Fig. 2 (b). Fig. 2 (c) shows the Rietveld refinement of the XRD spectrum for the H-Fe$_3$O$_4$. This secondary phase is discerned through the detection of specific diffraction peaks ($2\theta = 21.1381°$) that correspond to the goethite phase, as listed in the standard reference XRD pattern for goethite (ICDD-PDF card # 01-081-0462) [38].

The main peaks are described in Table 2 for both samples, while Fig. 2 shows that the diffraction peaks belong to Fe$_3$O$_4$ phase (ICDD-PDF card # 01-085-1436) [39]. The XRD analysis reveals a high degree of crystallinity, as evidenced by the sharp, well-defined peaks in the diffraction pattern. The XRD patterns obtained for both synthesis techniques exhibit remarkable similarities, strongly suggesting that the resulting materials possess nearly identical crystal structures. Nonetheless, minor variations in peak positions are observed, which could potentially be attributed to differences in crystallite size and the distinct methods of preparation employed. A comparative analysis of the XRD patterns for the synthesised R-Fe$_3$O$_4$ and H-Fe$_3$O$_4$ NPs indicates that the application of the reflux technique does not produce any significant impact on their crystal structure.

In order to obtain the average crystallite size of the samples, the diameter (d) is calculated using the Debye-Scherrer formula shown in Eq. (1):

$$d = \frac{K\lambda}{B\cos\theta} \tag{1}$$

where K is equal to 0.89 (Scherrer's constant), λ is the wavelength of X-rays, θ is the Bragg diffraction angle, and B is the full width at half-maximum (FWHM) of the intense diffraction peaks. The average crystallite sizes of the IONPs synthesised by the *hydrothermal* (H-Fe$_3$O$_4$) and the *reflux* (R-Fe$_3$O$_4$) methods were found to be $d = 35.56$ nm and
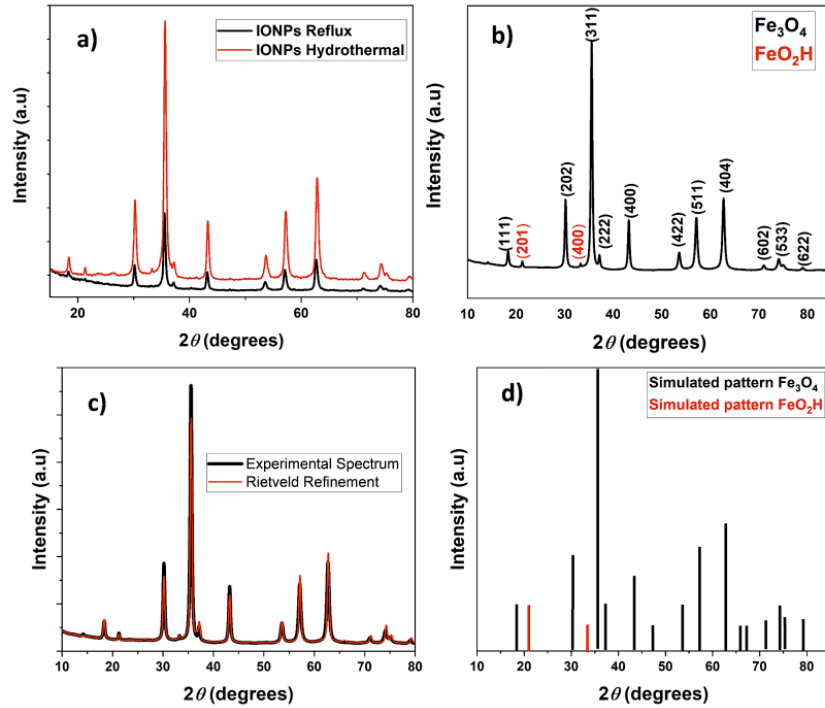
Figure 2: XRD analysis of the synthesised IONPs, where (a) XRD spectra for both materials; (b) peak identification for the IONPs synthesised with the hydrothermal method; (c) Rietveld refinement; and (d) simulated patterns for both phases.

Table 2
List of the XRD peaks for both samples: R-Fe$_3$O$_4$ (*Reflux method*), and H-Fe$_3$O$_4$ (*Hydrothermal method*).

IONPs (Reflux)				IONPs (Hydrothermal)			
Sample	Pos. (2θ)	d-spacing (Å)	hkl	Sample	Pos. (2θ)	d-spacing (Å)	hkl
R-FeO$_4$	18.3124	4.84481	111	H-FeO$_4$	18.3243	4.84170	111
R-FeO$_4$	21.1381	4.20312	110	H-FeO$_4$	21.2447	4.18226	110
R-FeO$_4$	30.1029	2.96872	220	H-FeO$_4$	30.1544	2.96377	220
R-FeO$_4$	35.4037	2.53544	311	H-FeO$_4$	35.5022	2.52864	311
R-FeO$_4$	37.0983	2.42343	222	H-FeO$_4$	37.1264	2.42166	222
R-FeO$_4$	43.0912	2.09926	400	H-FeO$_4$	43.1547	2.09632	400
R-FeO$_4$	53.4428	1.7152	422	H-FeO$_4$	53.5285	1.7197	422
R-FeO$_4$	56.9084	1.61807	511	H-FeO$_4$	57.0508	1.61436	511
R-FeO$_4$	62.6069	1.48380	440	H-FeO$_4$	62.6268	1.48337	440

d = 31.57 nm, respectively. These findings are consistent with previous studies on magnetite NPs synthesised using similar methods, which have reported crystallite sizes in the range of 20–30 nm and high phase purity [40, 41].

3.2. Scanning electron microscopy

The scanning electron microscopy (SEM) micrographs in Fig. 3 show the surface morphology of the NPs synthesised by the reflux and the hydrothermal techniques. In both cases, the particles present a close-to-spherical shape, with a tendency for agglomeration. However, the reflux method appears to produce some NPs with more elongated shapes.

Typical diameters of synthesised NPs are within 65 ± 10 nm, with some agglomerates in the range of 200 nm.

The elemental composition of the IONPs is determined using energy-dispersive X-ray spectroscopy (EDX). The EDX spectrum of the R-Fe$_3$O$_4$ (see Fig. 4) suggests the presence of Fe and O elements. The peaks around 0.8, 6.2, and 7.1 keV are related to the binding energies of Fe, along with the peak of oxygen at 0.5 keV. The Cl signals originate from the FeCl$_2 \cdot 4$H$_2$O precursor used in the synthesis.

3.3. Fourier transform infrared spectroscopy

Fourier transform infrared (FTIR) spectroscopy can be used to obtain the material's chemical composition and

(a) R-Fe$_3$O$_4$ (*Reflux* synthesis).

(b) H-Fe$_3$O$_4$ (*Hydrothermal* synthesis).
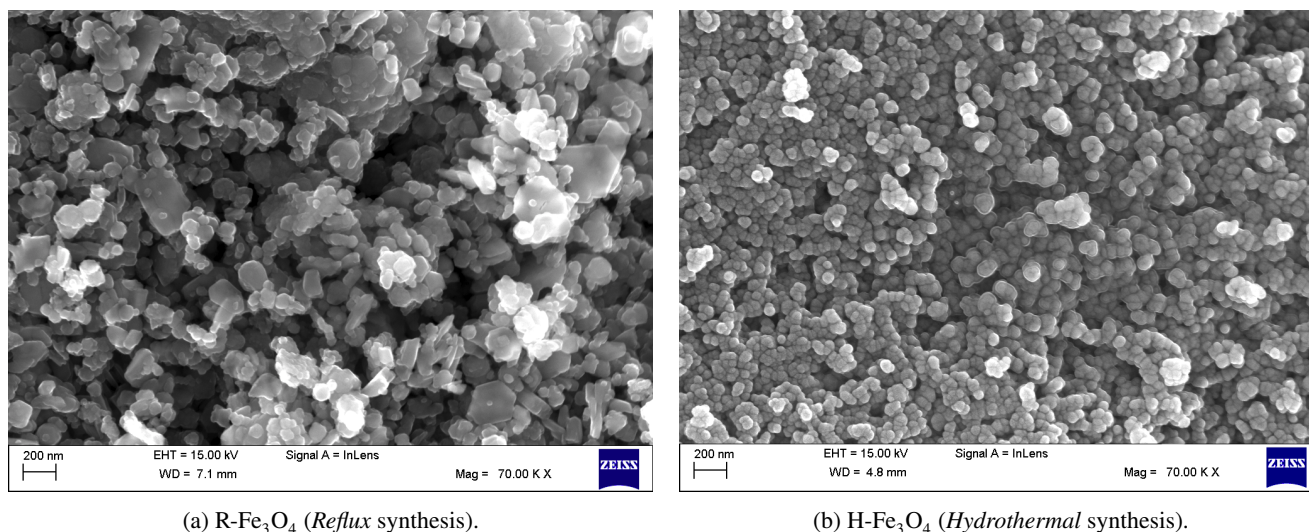
Figure 3: Morphology and elemental analysis of the synthesised Fe$_3$O$_4$ nanoparticles.
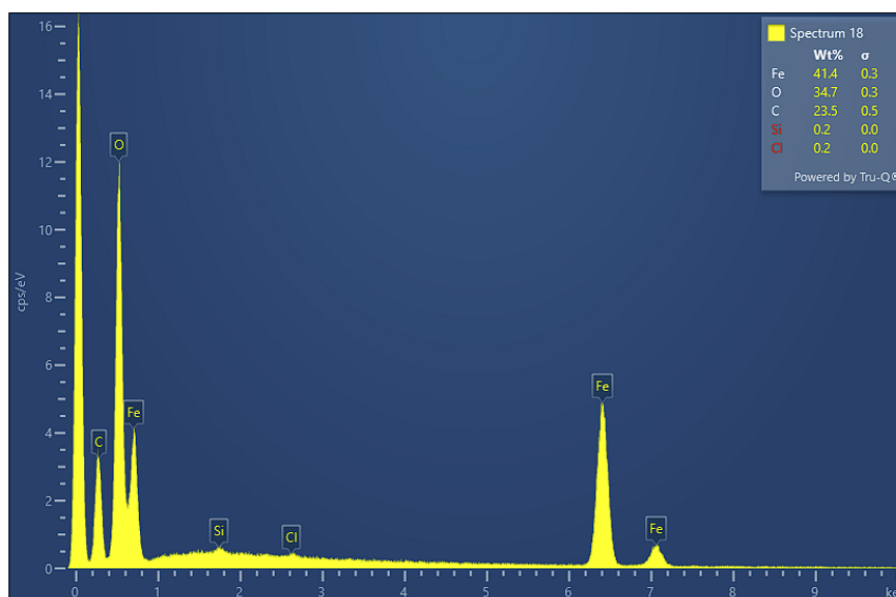
Figure 4: EDX Spectrum of the synthesised R-Fe$_3$O$_4$

.

physical state. Fig. 5 shows the FTIR spectra of the samples synthesised by the reflux (R-Fe$_3$O$_4$) and the hydrothermal (H-Fe$_3$O$_4$) methods. For the R-Fe$_3$O$_4$ sample, the wide peak at $3,123$ cm^{-1} is due to the O-H stretching mode [42]. Furthermore, the peaks at $1,651$ cm^{-1} and $1,455$ cm^{-1} are due to the aldehyde group (C=O stretch) [43]. The absorption peak at 800 cm^{-1} discovered the presence of aromatic C-H of aromatic compounds. The most interesting part of the IR spectra concerning ferrite is within the 800–500 cm^{-1} range, which is assigned to the vibrations of ions in the crystal lattice. Fe$_3$O$_4$ belongs to the class of inverse spinels. The bands at 543 cm^{-1} (H) and 545 cm^{-1} (R) are assigned to Fe^{3+}-O stretching vibrations inside the tetrahedral sites of the inverse spinel structure [44].

3.4. Foam drainage

Foam stability is defined as the time that the foam maintains its initial properties such as foaming degree, viscosity, wetting power, bubble size, and bubble distribution [45]. Therefore, foam drainage must be considered to study the stability of the Class A foam. Three different concentrations of the R-Fe$_3$O$_4$ and H-Fe$_3$O$_4$ are used to study their effect on the foam drainage. As can be observed in Fig. 6, the drainage time is prolonged for all concentrations, therefore increasing the foam strength and stability. The main mechanism suggested for NPs to improve foam stability is the adsorption at the gas–liquid interface, making the films more stable [22]. In the absence of NPs, the liquid is separated from the gas phase faster, indicating higher disproportionation of the

Table 3
Foam drainage times at different concentrations of synthesised H-Fe$_3$O$_4$ into Class A foam solutions.

IONPs Concentration Hydrothermal (wt%)	Class A Foam Concentrate (%)	Drainage time mean (s) $t_{25\%}$ (s)	Drainage time mean (s) $t_{50\%}$ (s)	Drainage time mean (s) $t_{75\%}$ (s)
0	0.6	157 (2.00)	282 (1.53)	441 (3.00)
0.025	0.6	170 (2.08)	303 (2.00)	518 (2.51)
0.05	0.6	175 (2.00)	309 (2.08)	551 (2.00)
0.1	0.6	162 (2.05)	299 (2.00)	560 (1.63)
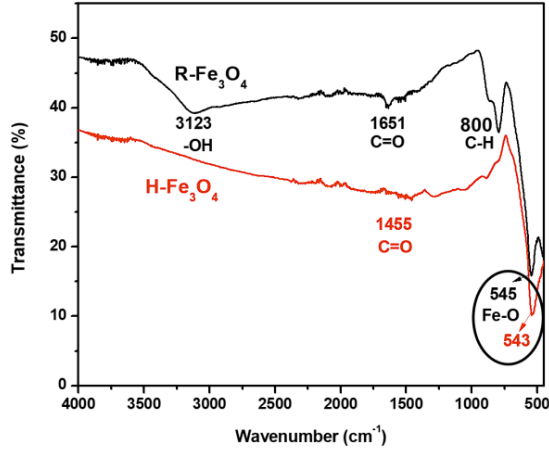
**Figure 5**: FTIR spectra of the synthesised IONPs.

bubbles [46]. Typically, the stability of firefighting foams is analysed for 25 % and 50 % drainage of the liquid out of the foam [10, 22, 47]. The rate of liquid drainage is determined at the times corresponding to 25 %, 50 %, and 75 % drainage. The *half-life of a foam* ($t_{50\%}$) is the time it takes for the foam in a solution to decrease to half of its initial volume. Table 3 and Table 4 present the mean sample foam drainage times and standard deviations at different IONPs concentrations for the NPs synthesised via the reflux and the hydrothermal methods, respectively. Each experiment was repeated three times. The sample standard deviation (s) for each set of three measurements is given by:

$$s = \sqrt{\frac{\sum_{i=1}^{n}(x_i - \overline{x})^2}{n-1}}$$

where:

- n is the number of measurements,
- x_i is the ith individual measurement,
- $\overline{x}$ is the mean of the measurements.

At $t_{25\%}$, the IONP concentration with the highest impact in delaying drainage is 0.05 wt%. At $t_{50\%}$, drainage is delayed more with R-Fe$_3$O$_4$ than with H-Fe$_3$O$_4$ NPs, which indicates higher foam stability. The delay time using R-Fe$_3$O$_4$ is 3.2 %
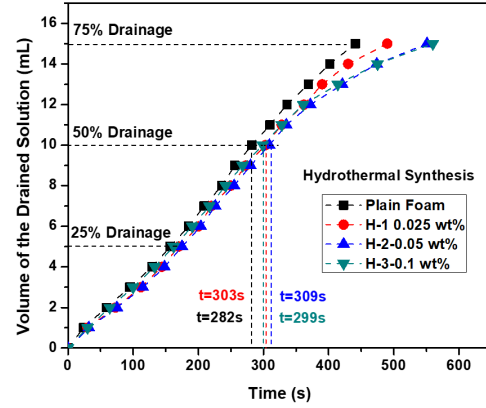
(a) H-Fe$_3$O$_4$ (*Hydrothermal* synthesis).
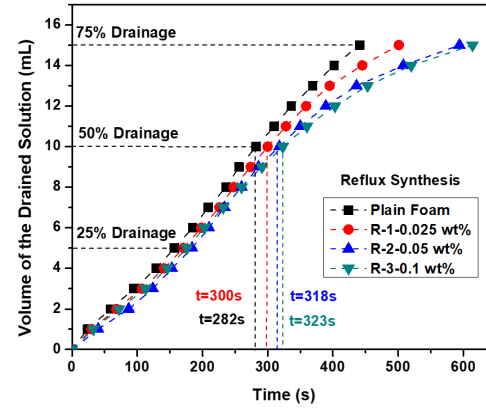
(b) R-Fe$_3$O$_4$ (*Reflux* synthesis).

Figure 6: Influence of synthesised IONPs on foam drainage.

longer than the one using H-Fe$_3$O$_4$. At $t_{75\%}$, when most of the liquid has been drained out of the foam due to gravity, 0.1 wt% concentration seems to stabilise the foam solution in both cases, providing more time to separate the gas and the liquid phases. This may be attributed to the IONPs at 0.1 wt% concentration being more tightly dispersed on the bubble surface [2]. The increase of $t_{50\%}$ for 0.1 wt% concentration is lower for the hydrothermal than for the refulx method. The increased collision probability of IONPs at higher concentrations may lead to a decrease in their dispersity, which may cause some agglomeration [2].

Table 4
Foam drainage times at different concentrations of synthesised R-Fe$_3$O$_4$ into Class A foam solutions.

IONPs Concentration Reflux (wt%)	Class A Foam Concentrate (%)	Drainage time mean (s) $t_{25\%}$ (s)	Drainage time mean (s) $t_{50\%}$ (s)	Drainage time mean (s) $t_{75\%}$ (s)
0	0.6	157 (2.00)	282 (1.53)	441 (3.00)
0.025	0.6	171 (2.05)	300 (3.30)	501 (2.49)
0.05	0.6	184 (2.16)	318 (3.09)	594 (3.74)
0.1	0.6	176 (2.62)	323 (2.05)	614 (2.16)
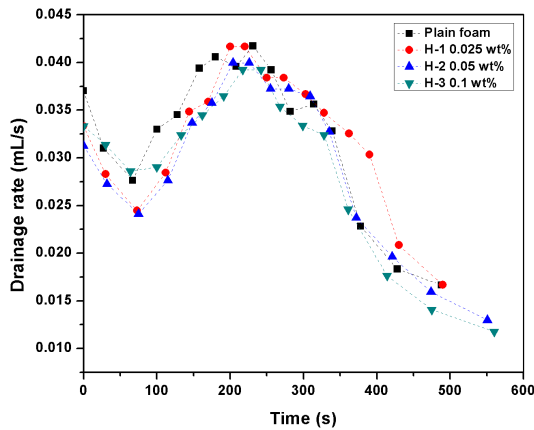
(a) H-Fe$_3$O$_4$ (*Hydrothermal* synthesis).
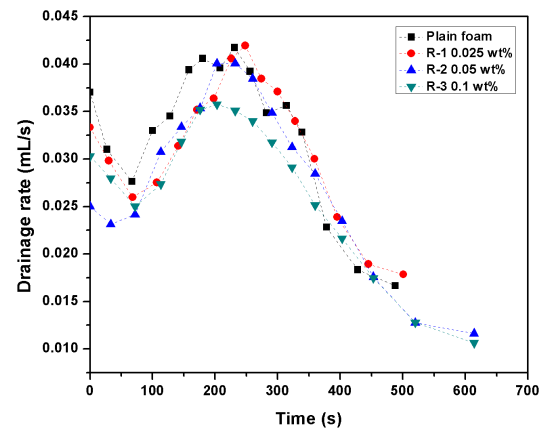
(b) R-Fe$_3$O$_4$ (*Reflux* synthesis).

Figure 7: Drainage rate curves over time for plain foam and for foams treated with different concentrations of IONPs.

The foam drainage rate is shown in Fig. 7, calculated for each foam sample as the derivative of the volume of the drained solution with respect to time. Fig. 7 (a) shows the drainage rate curves for the plain foam and for the foams enhanced with H-Fe$_3$O$_4$ NPs at the three concentrations, whilst Fig. 7 (b) shows the same for R-Fe$_3$O$_4$ NPs. As can be observed, the plain foam exhibits the highest drainage rates at the early stages of the experiment (until around 230 s), which indicates that the presence of IONPs enhances foam stability. In fact, Table 3 and Table 4 show that $t_{75\%}$ consistently increases with increasing concentrations. The same is true for $t_{50\%}$ (half-life), except for 0.1 wt% H-Fe$_3$O$_4$.

4. Identification of the interactions between the IONPs and class A foam

4.1. Influence of particle size distribution and zeta potential on foam stability

The particle size distribution and zeta potential in the foam liquid are closely related to foam stability [10, 48, 49]. Thus, for an in-depth understanding of the effect of adding IONPs to class A foams, the relation between their concentration and zeta potential in the foam liquid must be studied. To this end, a foam solution was prepared in a plastic container at 0.6 % of commercial foam concentrate,

as recommended by the supplier, and stirred with different concentrations of IONPs in the range of 0–0.1 wt%. The dispersion of the NPs was ensured by ultra-sonication for 40 min, then using an overhead stirrer to complete the homogenisation of the sample.

Table 5 shows the average zeta potential values and particle size of IONPs when added to the foam solution. The zeta potential of the plain foam solution was found to be positive at +0.86 mV, indicating that it is relatively close to the isoelectric point. This zeta potential suggests that the foam has thin cell walls [50], which is not optimal for its stability. As can be observed, when increasing the IONPs concentration, the zeta potential values increase for the foam solutions prepared using either technique. The higher absolute value of the zeta potential the more strongly the particles repel each other, and the more stable the dispersion is [51, 52]. Particles with zeta potentials in the ±30 mV range are considered to be unstable with respect to aggregation. The values observed in Table 5 are within the expected range, and hence aggregation of the NPs should be expected [53]. The hydrothermal particles look smaller under SEM for the same magnification, as can be observed in Fig. 3. Fig. 8 shows higher average hydrodynamic particle size at 0.1 wt% concentration for H-Fe$_3$O$_4$, which indicates greater agglomeration of NPs synthesised using the hydrothermal method.

Table 5
Zeta potential and particle diameter of IONPs at different concentrations for hydrothermal and reflux methods.

| IONPs Concentration (wt%)	Zeta Potential mean (s) (mV)	Average particle size (nm)
0	0.86 (0.19)	N/A
H-0.025	−18.51 (0.99)	1658
H-0.05	−17.43 (0.85)	2564
H-0.1	−10.20 (0.92)	3306
R-0.025	−28.78 (2.06)	1681
R-0.05	−14.60 (0.09)	2096
R-0.1	−8.80 (0.60)	2232

This is obtained by means of DLS. Thus, the average hydrodynamic H-Fe$_3$O$_4$ particle size is 3, 306 nm while that of the R-Fe$_3$O$_4$ particle is 2, 232 nm. At these concentrations, the IONPs behave as large particle aggregates, and may be deposited faster than the flow of the liquid and get trapped in the foam network [1].
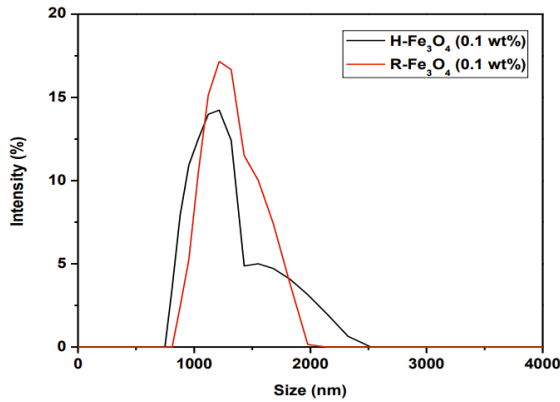
Figure 8: Average particle size showing IONPs agglomeration in Class A foam solution at 0.1 wt%, obtained by DLS.

The addition in increasing concentrations of H-Fe$_3$O$_4$ NPs resulted in decreasing the zeta potential absolute value from 18.51 mV to 10.2 mV, whereas the addition of R-Fe$_3$O$_4$ NPs led to decreasing the zeta potential absolute value from 28.78 mV to 8.8 mV. The decreasing absolute value of the zeta potential suggests that the class A foam surfactant is adsorbed in the surfaces of the NPs [15, 54]. A higher zeta potential indicates a greater degree of electrostatic repulsion between the particles, which makes the dispersion more stable [11, 55] . A corresponding average particle size increase is observed as a consequence of the adsorbed NPs. Particle foaming agents are characterised by their strong adsorption energy at the gas-water interface, which means that they have a high adsorption heat [11]. This makes the adsorption at the interface irreversible, meaning that the particles will stay attached to the interface once they are adsorbed.

Fig. 9 shows the complete distribution of IONPs in the solutions at different concentrations. Particles are seen to be uniformly suspended, ensuring homogeneity.
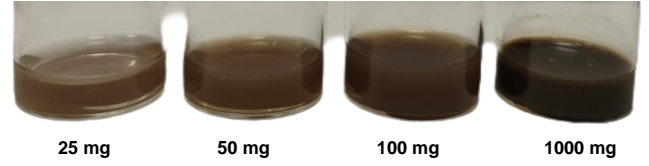
Figure 9: Solutions of IONPs at various concentrations. From left to right: 25 mg (0.025 wt%), 50 mg (0.05 wt%), 100 mg (0.1 wt%), and 1000 mg (1.0 wt%).

The average hydrodynamic particle size is seen to increase as the NP concentrations increase, indicating higher particle aggregation at higher concentrations [21]. However, there must be a uniform accumulation of the NPs around the foam lamellae as it does not promote foam stability [21]. High accumulation of the NPs end up promoting inter-bubble diffusion and accelerate liquid drainage by applying gravitational forces to the generated bubbles [21, 56].

4.2. Effect of IONPs concentration on foam surface tension

In order to investigate the effect of IONPs on the surface tension of the foam solutions, the pendant drop tensiometry was utilised [23]. The shape that a droplet suspended from a needle takes is a balance between the interfacial tensions favoring the formation of a spherical droplet, and gravity acting so as to deform the droplet from the spherical morphology. Pendant drop tensiometry makes use of an image capturing the adopted morphology of the deposited droplet to extract a value for the interfacial tension of the system as shown in Figs. 10 and 11. The summary of the pressure forces in equilibrium on a pendant drop includes a Laplace and a hydro-static term, presented in Eq. (2):

$$\gamma C = \rho g z \tag{2}$$

where γ (mN/m) is the interfacial tension, C (m^{-1}) is the droplet's surface curvature, and ρ (g/cm^3) is the density. Expressing the curvature around the z-axis in a cylindrical coordinate system, and defining r_z and r_{zz} as in Eq. (3), C can be expressed as in Eq. (4).
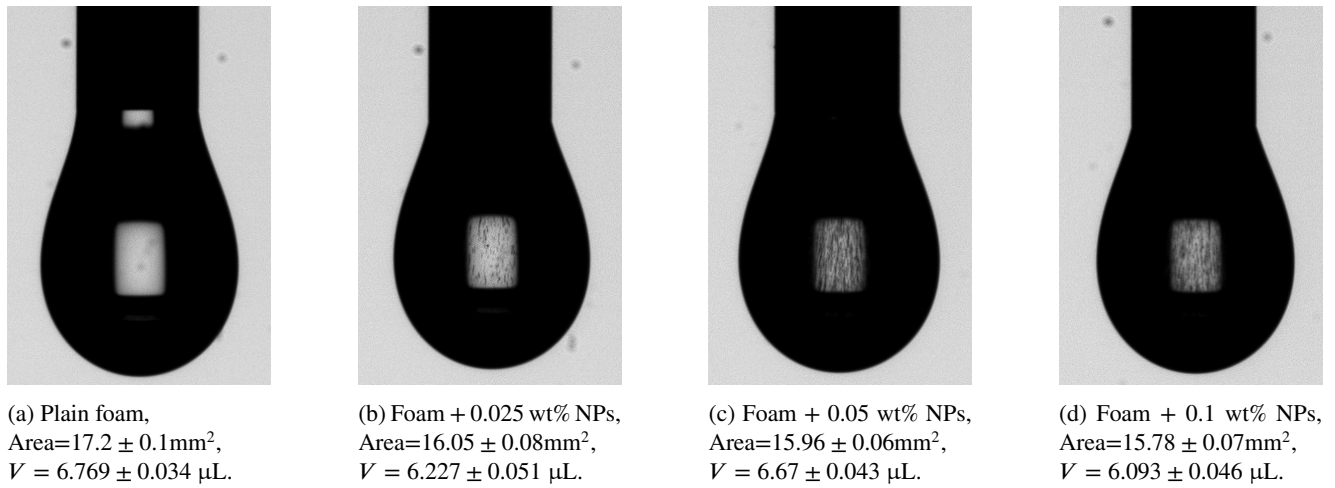
$$r_z = \frac{\mathrm{d}r}{\mathrm{d}z}, \qquad r_{zz} = \frac{\mathrm{d}^2 r}{\mathrm{d}z^2} \tag{3}$$

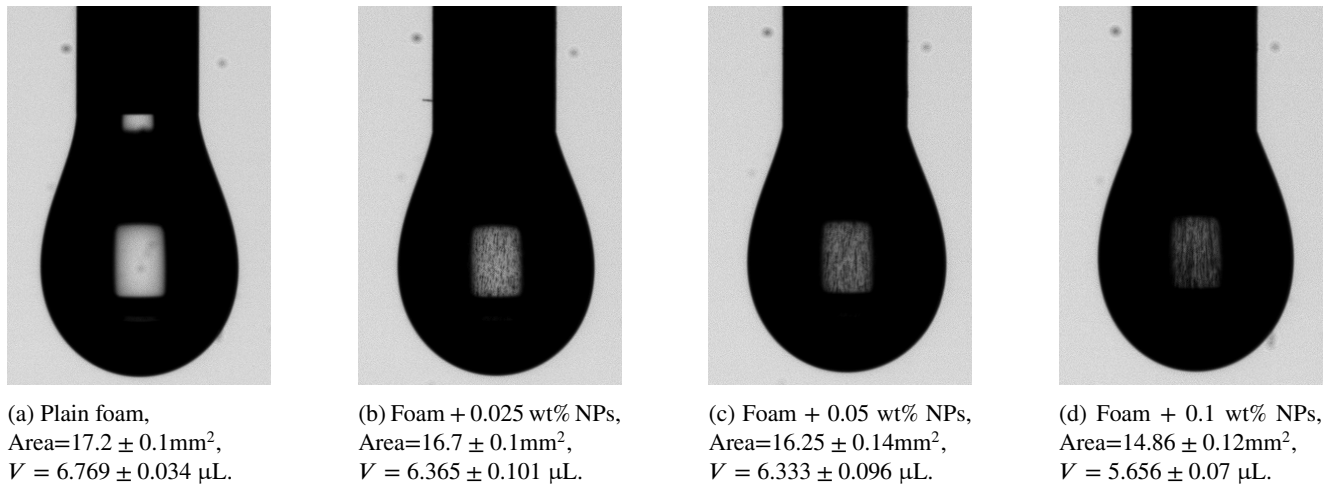$$C = -\frac{r_{zz}}{\left(1 + r_z^2\right)^{3/2}} + \frac{1}{r\left(1 + r_z^2\right)^{1/2}} \tag{4}$$

When conducting a pendant drop measurement, the interfacial tension term is varied such that a value that satisfies the above equation for the given droplet is met.

Figs. 10 and 11 show the different droplets formed from the syringe needle until just before detached from the needle

(a) Plain foam,
Area=17.2 ± 0.1mm^2,
$V = 6.769 \pm 0.034$ µL.

(b) Foam + 0.025 wt% NPs,
Area=16.05 ± 0.08mm^2,
$V = 6.227 \pm 0.051$ µL.

(c) Foam + 0.05 wt% NPs,
Area=15.96 ± 0.06mm^2,
$V = 6.67 \pm 0.043$ µL.

(d) Foam + 0.1 wt% NPs,
Area=15.78 ± 0.07mm^2,
$V = 6.093 \pm 0.046$ µL.

Figure 10: Water droplets analysed by pendant drop method at different concentrations of IONPs (Hydrothermal synthesis).

(a) Plain foam,
Area=17.2 ± 0.1mm^2,
$V = 6.769 \pm 0.034$ µL.

(b) Foam + 0.025 wt% NPs,
Area=16.7 ± 0.1mm^2,
$V = 6.365 \pm 0.101$ µL.

(c) Foam + 0.05 wt% NPs,
Area=16.25 ± 0.14mm^2,
$V = 6.333 \pm 0.096$ µL.

(d) Foam + 0.1 wt% NPs,
Area=14.86 ± 0.12mm^2,
$V = 5.656 \pm 0.07$ µL.

Figure 11: Water droplets analysed by pendant drop method at different concentrations of IONPs (Reflux synthesis).

tip. The addition of IONPs reduces the overall mean area of the droplets. The mean area of bubbles decreases with increasing IONPs concentration, indicating smaller droplet sizes with higher concentrations of NPs. This drop can be attributed to the surface activity where the IONPs are adsorbed in the air-liquid interface and tend to modify the surface tension, which leads to the formation of smaller and more stable droplets. Moreover, the mean volume of bubbles (V) decreases with increasing IONPs concentration, which is consistent with the decrease in mean droplet area. Additionally, electrostatic or steric stabilisation provided by NPs can maintain smaller droplet sizes by preventing droplet coalescence [57].

Having explored the influence of IONPs on the droplet shape mean area in DSA measurements, it is essential to examine their impact on the surface tension of the foam solution. Fig. 12 shows the equilibrium surface tension of the plain foam solution, as well as those of the solution with three concentrations of H-Fe$_3$O$_4$ and R-Fe$_3$O$_4$ NPs (i.e. seven samples). Measurements were taken once the system reached steady state, established to be after 120 s (when

readings stabilised). As can be observed, the addition of IONPs to the foam solution results in a decrease in the equilibrium surface tension compared to the plain foam solution, which is significant to enhance foam properties [58, 59]. Lower equilibrium surface tension reduces the energy required to create new air–liquid interfaces, facilitating the formation of foam with smaller and more stable bubbles [60]. At low concentrations of up to 0.050 wt%, NPs are likely adsorbing at the air–liquid interface. However, as the concentration increases (beyond 0.05 wt%), the surface may become saturated. In such a case, additional NPs are less likely to adsorb at the interface [61]. The surface tension is notably highest for the plain foam, confirming that the addition of IONPs modifies the air–liquid interfacial properties [62]. Further studies on different concentrations are required to investigate the values leading to minimum surface tension, whilst the IONPs synthesised using the hydrothermal method seem to be more effective in lowering the surface tension. The higher surface tension at higher concentrations may be due to the surfactant adsorption on the NPs and depletion on the air-water interface [23].
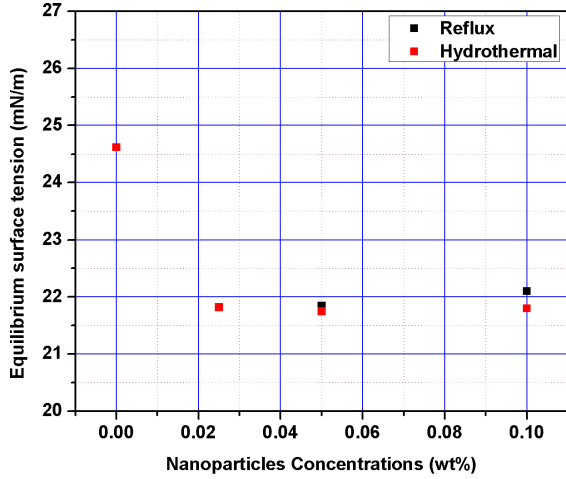
Figure 12: Equilibrium surface tension of foam solution with different concentrations of IONPs synthesised using reflux and hydrothermal methods (single experiment per concentration).

4.3. Bubble surface morphology

Foam coarsening is treated as gas diffusing from the gas bubbles into the surrounding liquid solution. The gas is transferred from smaller to bigger bubbles, leading to the disappearance of the smaller ones [4, 6, 7]. Foams presenting higher stability are able to better resist the effects of the foam coarsening and bubble coalescence, which results in longer foam half-life. In this work, the morphology of the bubbles is analysed using a digital microscope in order to study how the foam coarsening evolves in time.

Immediately after generating the foam using the double syringe technique, a small quantity was expelled from the syringe onto the centre of the glass microscope slide, promptly placing it under the microscope. Images of the foam were captured at different times to observe changes and gather data on foam characteristics.

Two images were recorded per sample, one immediately after foam generation and the other 10 min later. The length of the study is set to 10 min to align with the approximate time that the foam takes to reach its 75 % drainage time ($t_{75\%}$) [21]. The morphology of the bubbles immediately after foam generation and 10 min later are shown in Figs. 13 (a)–(b) for the plain foam, Figs. 13 (c)–(d) for 0.1 wt% H-Fe$_3$O$_4$, and Figs. 13 (e)–(f) for 0.1 wt% R-Fe$_3$O$_4$.

The average bubble size was determined using ImageJ [63]. An image of the foam at 10× magnification was analysed. The analysis revealed that a total of 526 bubbles were detected in the foam sample in Fig. 13 (a). The area of each individual bubble was calculated by ImageJ as in Eq. 5:

$$\text{Area} = \text{Number of Pixels} \times \text{Area per Pixel}. \tag{5}$$

Given the area (A) of a circular bubble, its diameter can be calculated as in Eq. (6):

$$d = 2\sqrt{\frac{A}{\pi}}. \tag{6}$$

In this study, each bubble's area is measured in square micrometers (μm^2) and its diameter is calculated as in Eq. 6. The average diameter and its standard deviation are then calculated to characterise the average size distribution of the bubbles in Table 6.

The destabilisation process of the foam depends on the coalescence (rupture of films between bubbles), and on the coarsening (gas diffusion between bubbles due to pressure difference). After 10 min have elapsed from the foam generation, the bubbles are seen to have formed a polyhedral shape and and to have increased their average size. By comparing Figs. 13 (a) and (b), it can be observed that the plain foam's bubble distribution changes from circular at the beginning to polyhedral after 10 min, indicating a low liquid volume fraction (ϕ) in the foam [6]. This behaviour can be related to the gas diffused between bubbles of different radius due to differences in the Laplace pressure. The gas is transferred from smaller to bigger bubbles, leading to the disappearance of the former [13].

Initially, the plain foam had 526 bubbles, number that drastically decreased to 34 after 10 min, with a significant increase in average bubble size from 5.5 µm to 25.81 µm. This suggests rapid bubble coalescence and foam destabilisation over time. In contrast, the enhanced foams with 0.1 wt% H-Fe$_3$O$_4$ and R-Fe$_3$O$_4$ NPs maintain the bubbles approximately spherical even after 10 min have elapsed since the foam generation, as shown in Figs. 13 (d) and (f). This indicates a delay in foam drainage, which is the result of a higher liquid volume fraction (ϕ) where the bubbles are spherical and move independently [6]. This suggests that the NPs are adsorbed to the bubble surface sufficiently fast, stabilising it, and thus limiting their deterioration. This result can be attributed to the foam solution's improved surface dilational viscoelasticity as a result of NPs adsorption and accumulation on the bubble surface and plateau border [21].

The foam coarsening process was quantitatively analysed using the bubble size distribution across three different samples. Fig. 14 displays the size distributions at $t = 0$ min and $t = 10$ min after foam generation for the plain foam, for the foam enhanced with 0.1 wt% H-Fe$_3$O$_4$ (H-3), and for the foam enhanced with 0.1 wt% R-Fe$_3$O$_4$ (R-3). At $t = 0$ min, the average bubble diameters (D) were 52.61 µm, 61.78 µm, and 60.35 µm for the plain foam, H-3, and R-3, respectively. The distribution indicates that bubbles were initially small, with the majority of bubbles under 100 µm in diameter for all concentrations. The addition of NPs did not significantly alter the initial bubble sizes and distributions. At $t = 10$ min, the foam coarsening process can be observed. The average bubble diameter of plain foam increased significantly to 335.55 µm, indicating rapid coarsening. For the H-3 sample, the average bubble diameter increased to 113.31 µm. Similarly, the average bubble diameter reached 118.91 µm for the R-3 sample. Thus, both NP-enhanced foams exhibited lower rates of coarsening compared to the plain foam, with most bubbles remaining below 300 µm.

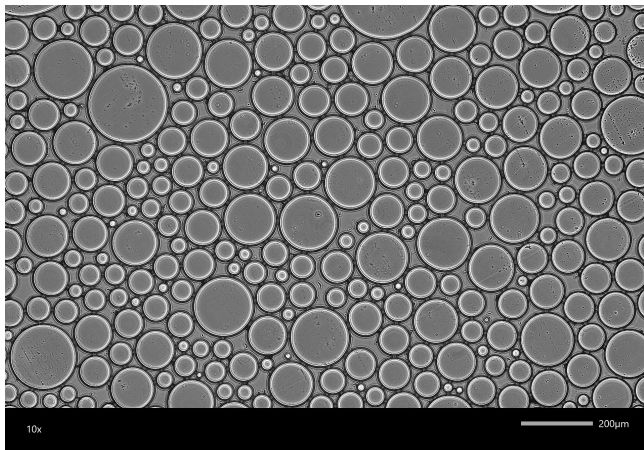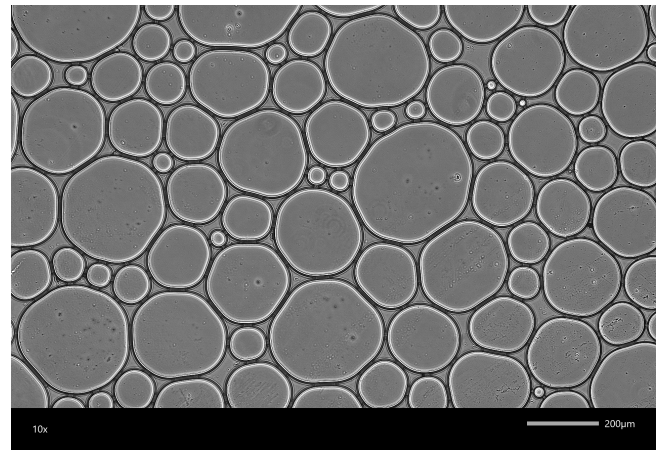Results demonstrate that, while bubble coarsening occurred in all samples, the presence of NPs notably slowed the
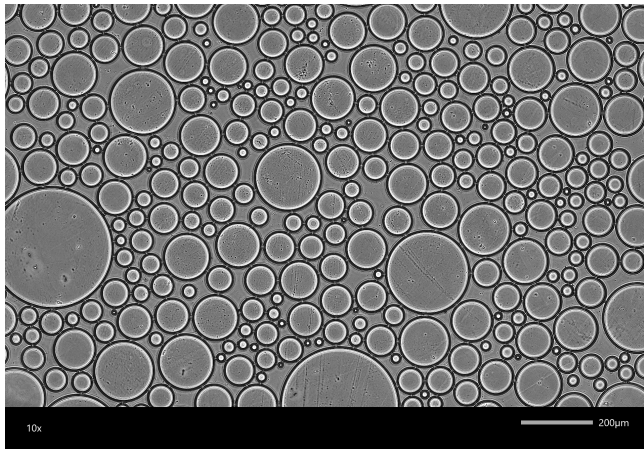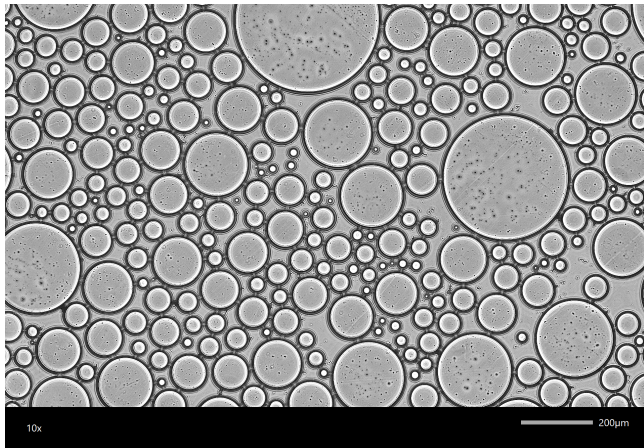
(a) Plain foam, $t = 0$ min.
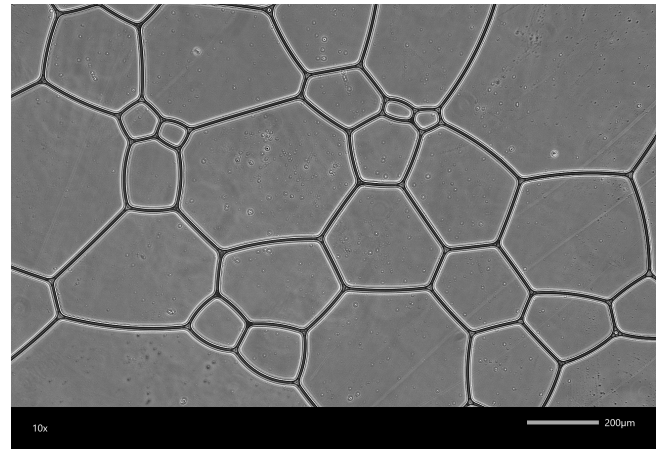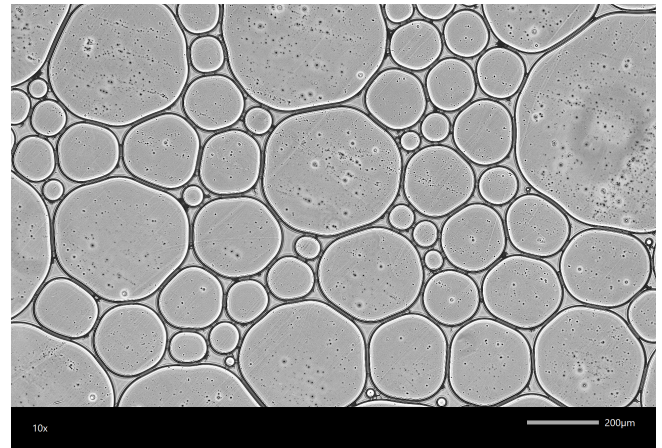
(b) Plain foam, $t = 10$ min.

(c) Enhanced Foam, 0.1 wt% H-Fe$_3$O$_4$ NPs, $t = 0$ min.

(d) Enhanced Foam, 0.1 wt% H-Fe$_3$O$_4$ NPs, $t = 10$ min.

(e) Enhanced Foam, 0.1 wt% R-Fe$_3$O$_4$ NPs, $t = 0$ min.

(f) Enhanced Foam, 0.1 wt% R-Fe$_3$O$_4$ NPs, $t = 10$ min.

Figure 13: Foam bubble morphologies (10× magnification) at $t = 0$ min (foam generation) and $t = 10$ min after foam generation for plain foam, and for foam enhanced with 0.1wt% Fe$_3$O$_4$ synthesised using the *Hydrothermal* (H) and the *Reflux* (R) methods.

process. At $t = 10$ min, the plain foam showed a considerable increase in larger bubbles, with many exceeding 300 μm in diameter, whereas the NP-enhanced foams maintained a narrower size distribution with fewer large bubbles.

Experimental results show that the addition of 0.1 wt% NPs effectively reduce the foam coarsening rate, stabilising the bubble structure over time. A combined analysis of these results with those from the foam drainage experiments

Table 6
Comparison of bubble sizes in plain foam versus foam enhanced with nanoparticles.

Description	Time (min)	Number of Bubbles	Average Bubble Size (μm)
Plain foam	0	526	5.5 ± 3.74
Plain foam	10	34	25.81 ± 14.74
Enhanced foam, 0.1 wt% H-Fe_3O_4 NPs	0	539	5.22 ± 3.5
Enhanced foam, 0.1 wt% H-Fe_3O_4 NPs	10	132	11.59 ± 8.14
Enhanced foam, 0.1 wt% R-Fe_3O_4 NPs	0	429	5.75 ± 4.58
Enhanced foam, 0.1 wt% R-Fe_3O_4 NPs	10	111	11.93 ± 10.38

Figure 14: Bubble diameter distributions at $t = 0$ min (foam generation) and $t = 10$ min after foam generation for plain foam, and for foam enhanced with 0.1 wt% Fe_3O_4 synthesised using the *Hydrothermal* (H-3) and the *Reflux* (R-3) methods.

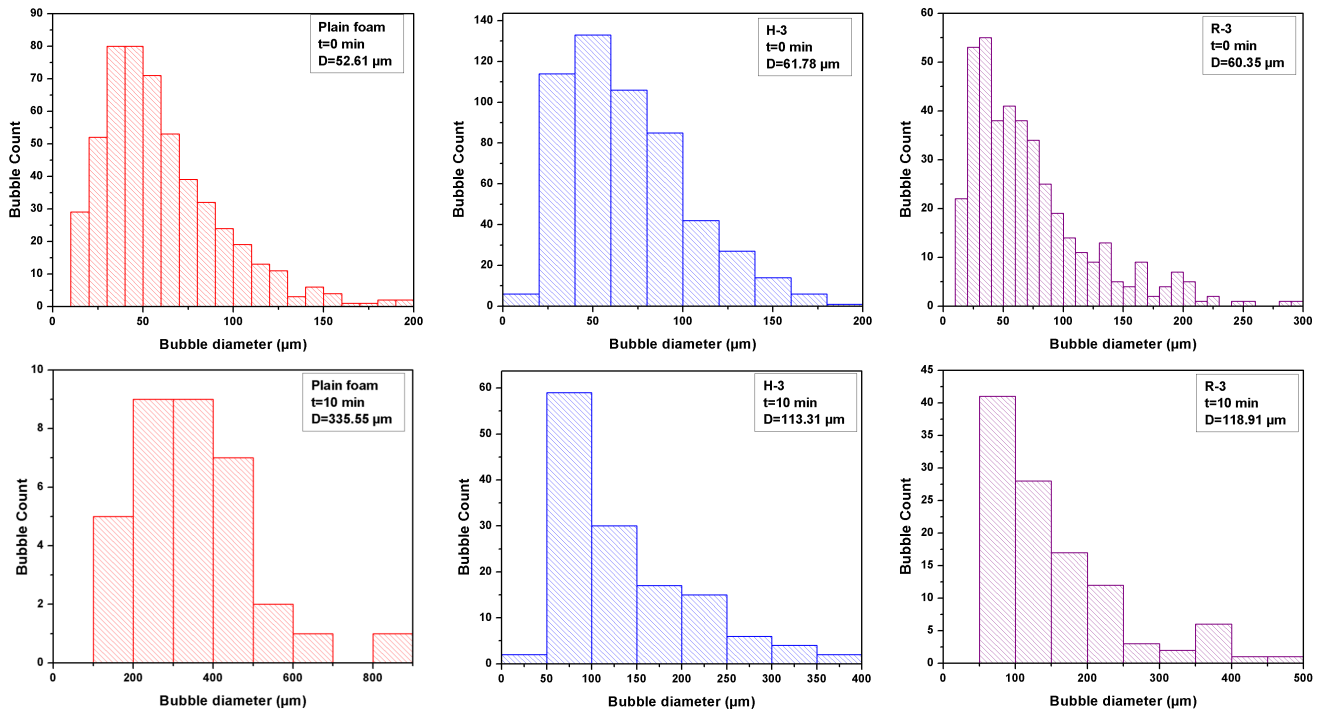indicates that a concentration of 0.1 wt% IONPs enhances foam stability by improving liquid retention.

4.4. Mechanisms of foam stability improvement

When the foam is generated, it is composed of individual bubbles that are separated by thin films of liquid, known as plateau borders (PBs) [22, 62]. These PBs are highly unstable and prone to rupture, which can cause the foam to collapse. This behaviour is caused as a combination of various factors, including capillary forces, gravity, and surface tension [64]. Generally, most of the liquid is found in the PBs. When four PBs join together, they form junctions or nodes (see Fig. 15). A mechanism to stabilise these PBs is the addition of nanomaterials [6]. Fig. 15 illustrates the main mechanisms by which IONPs stabilise the foam lamellae and decelerate foam drainage and coarsening. When NPs are introduced to the foam, they can aggregate at the plateau borders due to their high surface area and surface energy.

Most NPs tend to aggregate once they are hydrated [65]. The NPs aggregate easily because they have a large ratio of surface area to volume (due to the small particle size); therefore, possess high surface energies and consequently create an aggregate form to minimise these surface energies [66]. This aggregation can cause them to form a physical barrier that reinforces the plateau borders and prevents them from rupturing [14]. During this process, the aggregated IONPs delay the flow of the liquid downwards the Plateau borders, thus providing a steric barrier to film thinning and inter-bubble diffusion [21]. Moreover, the aggregated IONPs can form a layered structure inside the thinning film, thus stabilising it by the so-called oscillatory structural force [67]. The thinning and stability of the aqueous films separating the foam bubbles are crucial for coalescence and foam collapse.

Finally, the adsorption of the NPs on the bubble interface is irreversible, which implies that NPs are difficult to detach from the interfaces, thus impeding bubble coalescence and reducing foam drainage. In summary, IONPs can aggregate at the PBs of foam bubbles to stabilise them by forming a protective layer that prevents the liquid films from breaking.
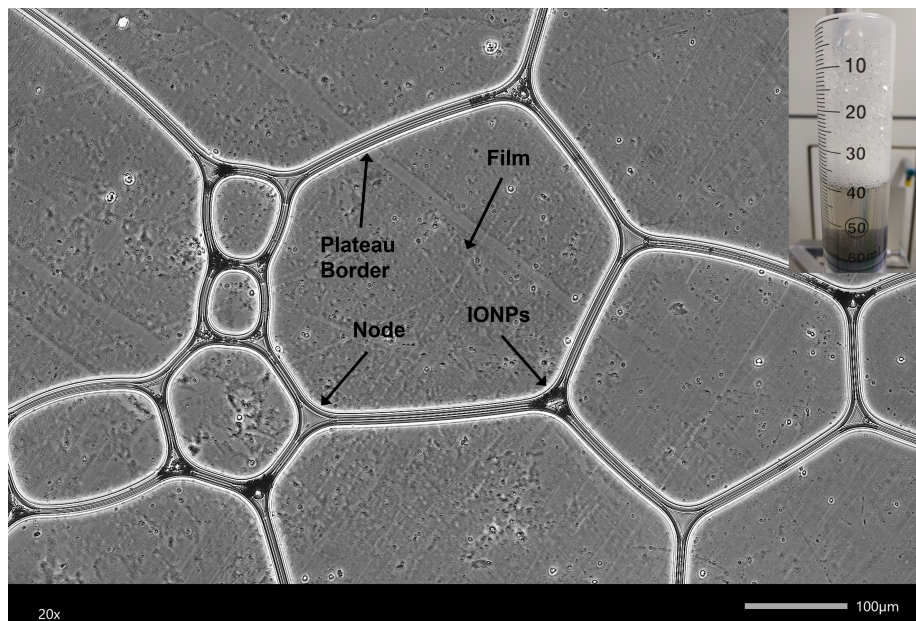
Figure 15: Illustration of an aqueous foam–NPs system. The drainage time of the film may be reduced due to the accumulation of IONPs in the plateau borders.

This mechanism can improve the effectiveness and efficiency of firefighting foam.

5. Conclusions

In this paper, the effect of iron oxide nanoparticles (IONPs) synthesised by two different methods, namely the *Reflux* and the *Hydrothermal* methods, on the stability of a commercial Class A foam was systematically investigated. It was found that the addition of Fe_3O_4 nanoparticles (NPs) at certain concentrations into the foam solution improves foam stability. In the absence of NPs, bubble sizes are larger and fewer, thus indicating a high rate of bubble coalescence and coarsening. The foam half-life was increased in both cases due to the accumulation of NPs in the foam network, thus providing an interfacial shield to delay foam drainage.

An analysis of the morphology of the bubbles on the micro-scale suggests that the NPs assemble at the plateau borders and nodes of the bubbles to reduce coarsening and disproportionation. As a result, the foam stability improves due to the adsorption of the NPs on the gas-liquid interface. The results regarding the wetting characteristics of the IONPs show that they decrease the surface tension of the foam solution, indicating that the NPs have changed the air-liquid interfacial properties. The lowest surface tension was achieved at the lowest concentration of IONPs, while higher concentrations resulted in higher surface tension due to surfactant adsorption on IONPs and depletion at the air-water interface. Furthermore, it can be concluded that the reflux method is a more advantageous technique to use compared to the hydrothermal method, despite the lack of significant differences in the results obtained. This is because the reflux method is more cost-effective and time-efficient, which are

important factors to consider in laboratory settings. Furthermore, the reflux method requires fewer resources and is easier to perform, making it a more practical choice for routine experiments.

Therefore, it is recommended that the reflux method be utilised for future experiments that require similar conditions. Potential synergistic effects of IONPs with Class A foams may arise through the formation of a protective barrier layer on top of the surface of the foam. This has provided experimental support for the further study of IONPs by focusing on different grain sizes to assess foam stability. Future goals of the project include performing comparative small-scale fire experiments using conventional foams and foams enhanced with NPs at the most effective concentration.

CRediT authorship contribution statement

Ioannis Papagiannis: Conceptualization, Data curation, Formal analysis, Investigation, Methodology, Visualization, Writing. **Mauro S. Innocente:** Conceptualization, Data curation, Formal analysis, Funding acquisition, Methodology, Project administration, Resources, Supervision, Visualisation, Writing. **Joshua D. Davies:** Investigation, Visualization. **Joshua L. Ryan:** Investigation, Visualization. **Evangelos I. Gkanas:** Conceptualization, Formal analysis, Funding acquisition, Methodology, Project administration, Resources, Supervision, Visualization, Writing.

References

[1] A. L. Fameau, A. Salonen, Effect of particles and aggregated structures on the foam stability and aging, Comptes Rendus Physique 15 (2014) 748–760.

[2] B. Long, D. Wang, R. Niu, H. Song, Y. Ma, G. Qu, J. He, In-situ activation of nano-silica and its foam stabilization mechanism, Journal of Dispersion Science and Technology 41 (1) (2020) 72–80.

[3] Y. Sheng, M. Xue, Y. Wang, X. Zhai, S. Zhang, Q. Wang, L. Ma, X. Ding, X. Liu, Aggregation behavior and foam properties of the mixture of hydrocarbon and fluorocarbon surfactants with addition of nanoparticles, Journal of Molecular Liquids 323 (2021) 115070.

[4] K. M. Hinnant, M. W. Conroy, R. Ananth, Influence of fuel on foam degradation for fluorinated and fluorine-free foams, Colloids and Surfaces A: Physicochemical and Engineering Aspects 522 (2017) 1–17.

[5] G. L. Thomas, J. M. Belmonte, F. Graner, J. A. Glazier, R. M. C. de Almeida, 3D simulations of wet foam coarsening evidence a self similar growth regime, Colloids and Surfaces A: Physicochemical and Engineering Aspects 473 (2015) 109–114.

[6] D. Langevin, Aqueous foams and foam films stabilised by surfactants. Gravity-free studies, Comptes Rendus Mécanique 345 (2017) 47–55.

[7] Y. Lu, T. Wang, M. Pang, Z.-j. Tian, Preparation and high temperature resistance of a novel aqueous foam for fire extinguishing, Procedia engineering 211 (2018) 514–520.

[8] I. Tureková, K. Balog, The environmental impacts of fire-fighting foams, Research Papers Faculty of Materials Science and Technology Slovak University of Technology 18 (29) (2010) 111–120.

[9] K. M. Hinnant, S. L. Giles, E. P. Smith, A. W. Snow, R. Ananth, Characterizing the Role of Fluorocarbon and Hydrocarbon Surfactants in Firefighting-Foam Formulations for Fire-Suppression, Fire Technology 56 (2020) 1413–1441.

[10] R. Zhou, X. Dou, X. Lang, L. He, J. Liu, S. Mu, Foaming ability and stability of silica nanoparticle-based triple-phase foam for oil fire extinguishing: Experimental, Soft Materials 16 (4) (2018) 327–338.

[11] G. Wang, K. L. Wang, C. J. Lu, Advances of researches on improving the stability of foams by nanoparticles, in: IOP Conference Series: Materials Science and Engineering, Vol. 242, IOP Publishing, 2017, p. 012020.

[12] M. K. Memon, K. A. Elraies, M. I. A. Al-Mossawy, Surfactant screening to generate strong foam with formation water and crude oil, Journal of Petroleum Exploration and Production Technology 11 (2021) 3521–3532.

[13] Y. Fei, K. Pokalai, R. Johnson, M. Gonzalez, M. Haghighi, Experimental and simulation study of foam stability and the effects on hydraulic fracture proppant placement, Journal of Natural Gas Science and Engineering 46 (2017) 544–554.

[14] R. J. Pugh, Bubble and foam chemistry, Cambridge University Press, 2016.

[15] M. Zhao, R. Wang, C. Dai, X. Wu, Y. Wu, Y. Dai, Y. Wu, Adsorption behaviour of surfactant-nanoparticles at the gas-liquid interface: influence of the alkane chain length, Chemical Engineering Science 206 (2019) 203–211.

[16] R. Olawoyin, Nanotechnology: The future of fire safety, Safety science 110 (2018) 214–221.

[17] F. Dassenoy, Nanoparticles as Additives for the Development of High Performance and Environmentally Friendly Engine Lubricants, Tribology Online 14 (2019) 237–253.

[18] Z. Tianwei, Z. Cunwei, L. Hao, H. Zhiyue, Experimental investigation of novel dry liquids with aqueous potassium solution@ nano-sio2 for the suppression of liquid fuel fires: preparation, application, and stability, Fire Safety Journal 115 (2020) 103144.

[19] U. T. Gonzenbach, A. R. Studart, E. Tervoort, L. J. Gauckler, Tailoring the microstructure of particle-stabilized wet foams, (Langmuir) 23 (3) (2007) 1025–1032.

[20] Y. Yang, X. Wu, J. Zhang, F. Shang, F. Xiao, K. Li, X. Liu, Plateau boundary blocking effect of nano-sio2 on foam properties of gemini fluorocarbon and hydrocarbon surfactant mixed solution, Fire Safety Journal 142 (2024) 104019.

[21] N. Yekeen, A. K. Idris, M. A. Manan, A. M. Samin, A. R. Risal, T. X. Kun, Bulk and bubble-scale experimental studies of influence of nanoparticles on foam stability, Chinese Journal of Chemical Engineering 25 (3) (2017) 347–357.

[22] B. Tang, Z. Wu, Z.-h. Chen, Effect of nanosilica on foam and thermal stability of a foam extinguishing agent, Nanomaterials and Energy 6 (2) (2017) 67–73.

[23] Q. Sun, Z. Li, J. Wang, S. Li, B. Li, L. Jiang, H. Wang, Q. Lü, C. Zhang, W. Liu, Aqueous foam stabilized by partially hydrophobic nanoparticles in the presence of surfactant, Colloids and Surfaces A: Physicochemical and Engineering Aspects 471 (2015) 54–64.

[24] B. P. Binks, T. S. Horozov, Aqueous foams stabilized solely by silica nanoparticles, Angewandte Chemie International Edition 44 (24) (2005) 3722–3725.

[25] T. X. Phuoc, R.-H. Chen, Modeling the effect of particle size on the activation energy and ignition temperature of metallic nanoparticles, Combustion and Flame 159 (1) (2012) 416–419.

[26] X. Chen, Y. Yin, J. Lu, X. Chen, Preparation and properties of iron-based flame-retardant reinforcing agent, Journal of fire sciences 32 (2) (2014) 179–190.

[27] J. Cong, G. Yang, L. Zhao, Q. Zhang, et al., The Synergistic Smoke Suppression Effect Of Ferric Oxide On Flame Retardant Wood-Polyurethane Composites, Wood Research 63 (2) (2018) 305–320.

[28] X. Chen, L. Liu, C. Jiao, Influence of iron oxide brown on smoke-suppression properties and combustion behavior of intumescent flame-retardant epoxy composites, Advances in Polymer Technology 34 (4) (2015).

[29] H. Jiang, Y. Jiang, R. Fan, Extinguishing capability of novel ultra-fine dry chemical agents loaded with iron hydroxide oxide, Fire Safety Journal 130 (2022) 103578.

[30] E. I. Gkanas, In vitro magnetic hyperthermia response of iron oxide MNP's incorporated in DA3, MCF-7 and HeLa cancer cell lines, Central European Journal of Chemistry 11 (2013) 1042–1054.

[31] I. Papagiannis, M. S. Innocente, E. I. Gkanas, Synthesis and Characterisation of Iron Oxide Nanoparticles with Tunable Sizes by Hydrothermal Method, Materials Science Forum 1053 (2022) 176–181. doi:10.4028/p-0so8ha.

[32] Q. Kong, Y. Hu, L. Song, Y. Wang, Z. Chen, W. Fan, Influence of Fe-MMT on crosslinking and thermal degradation in silicone rubber/clay nanocomposites, Polymers for Advanced Technologies 17 (2006) 463–467.

[33] Y. Koshiba, M. Sugimoto, Fire-suppression capability of surfactant-free aqueous dispersions of submicron-sized ferrocene particles, Case Studies in Thermal Engineering 28 (2021) 101459.

[34] J. C. Voelkert, Fire and fire extinguishment a brief guide to fire chemistry and extinguishment theory for fire equipment service technicians.

[35] J. Shen, J. Liang, X. Lin, H. Lin, J. Yu, S. Wang, The flame-retardant mechanisms and preparation of polymer composites and their potential application in construction engineering, Polymers 14 (1) (2021) 82.

[36] K. Furusawa, T. Kawamura, Y. Akutsu, M. Arai, M. Tamura, Reaction of gas-phase radicals from combustion with radical scavengers, Atmospheric Environment 31 (20) (1997) 3363–3367.

[37] Forexpan | Angus Fire.

[38] J.-L. Hazemann, J. F. Bérar, A. Manceau, Rietveld studies of the aluminium-iron substitution in synthetic goethite, Materials Science Forum 79-82 (1991) 821–826.

[39] K. Yasuda, Y. Kitamoto, Fabrication of Fe3O4 nanorods designed for liquid-phase magnetic biosensing, in: AIP Conference Proceedings, Vol. 1929, AIP Publishing, 2018.

[40] S. Ge, X. Shi, K. Sun, C. Li, C. Uher, J. R. Baker Jr, M. M. Banaszak Holl, B. G. Orr, Facile hydrothermal synthesis of iron oxide nanoparticles with tunable magnetic properties, The Journal of Physical Chemistry C 113 (31) (2009) 13593–13599.

[41] S. A. Jayanthi, D. M. G. T. Nathan, J. Jayashainy, P. Sagayaraj, A novel hydrothermal approach for synthesizing α-Fe2O3, γ-Fe2O3 and Fe3O4 mesoporous magnetic nanoparticles, Materials Chemistry and Physics 162 (2015) 316–325.

[42] M. Yaghoobi, F. Asjadi, M. Sanikhani, A facile one-step green hydrothermal synthesis of paramagnetic Fe3O4 nanoparticles with

highly efficient dye removal, Journal of the Taiwan Institute of Chemical Engineers 144 (2023) 104774.

[43] Z. Salehnia, D. Shahbazi-Gahrouei, A. Akbarzadeh, B. Baradaran, S. Farajnia, M. Naghibi, Synthesis and characterisation of iron oxide nanoparticles conjugated with epidermal growth factor receptor (EGFR) monoclonal antibody as MRI contrast agent for cancer detection, IET nanobiotechnology 13 (4) (2019) 400–406.

[44] S. Li, T. Zhang, R. Tang, H. Qiu, C. Wang, Z. Zhou, Solvothermal synthesis and characterization of monodisperse superparamagnetic iron oxide nanoparticles, Journal of Magnetism and Magnetic Materials 379 (2015) 226–231.

[45] A. K. R. Choudhury, Process control in finishing of textiles, Process Control in Textile Manufacturing (2013) 363–427.

[46] T. B. J. Blijdenstein, P. W. N. D. Groot, S. D. Stoyanov, On the link between foam coarsening and surface rheology: Why hydrophobins are so different, Soft Matter 6 (2010) 1799–1808.

[47] J. Rakowska, Best practices for selection and application of firefighting foam, in: MATEC Web of Conferences, Vol. 247, EDP Sciences, EDP Sciences, 2018, p. 00014.

[48] M. R. Behera, S. R. Varade, P. Ghosh, P. Paul, A. S. Negi, Foaming in micellar solutions: Effects of surfactant, salt, and oil concentrations, Industrial & Engineering Chemistry Research 53 (48) (2014) 18497–18507.

[49] P. Wang, J. Wang, H. Zhang, Y. Dong, Y. Zhang, The role of iron oxides in the preservation of soil organic matter under long-term fertilization, Journal of Soils and Sediments 19 (2019) 588–598.

[50] W. Huo, X. Zhang, K. Gan, Y. Chen, J. Xu, J. Yang, Effect of zeta potential on properties of foamed colloidal suspension, Journal of the European Ceramic Society 39 (2-3) (2019) 574–583.

[51] E. Taboada, E. Rodriguez, A. Roig, J. Oro, A. Roch, R. N. Muller, New ultrasmall iron-oxide nanoparticles with high magnetisation as potential T1-MRI contrast agents for molecular imaging, arXiv preprint cond-mat/0611243 (2006).

[52] R. Muneer, M. R. Hashmet, P. Pourafshary, M. Shakeel, Unlocking the power of artificial intelligence: accurate zeta potential prediction using machine learning, Nanomaterials 13 (7) (2023) 1209.

[53] N. Raval, R. Maheshwari, D. Kalyane, S. R. Youngren-Ortiz, M. B. Chougule, R. K. Tekade, Importance of physicochemical characterization of nanoparticles in pharmaceutical product development, in: Basic fundamentals of drug delivery, Elsevier, 2019, pp. 369–400.

[54] H. Vatanparast, F. Shahabi, A. Bahramian, A. Javadi, R. Miller, The role of electrostatic repulsion on increasing surface activity of anionic surfactants in the presence of hydrophilic silica nanoparticles, Scientific Reports 8 (1) (2018) 7251.

[55] K. Vinothini, M. Rajan, Mechanism for the nano-based drug delivery system, in: Characterization and biology of nanomaterials for drug delivery, Elsevier, 2019, pp. 219–263.

[56] I. Kim, A. Taghavy, D. DiCarlo, C. Huh, Aggregation of silica nanoparticles and its impact on particle mobility under high-salinity conditions, Journal of Petroleum Science and Engineering 133 (2015) 376–383.

[57] Z. Briceño-Ahumada, J. F. A. Soltero-Martínez, R. Castillo, Aqueous foams and emulsions stabilized by mixtures of silica nanoparticles and surfactants: A state-of-the-art review, Chemical Engineering Journal Advances 7 (2021) 100116.

[58] Q. Li, K. Qiu, C. Li, H. Li, M. Zhang, H. Liu, Stability and rheological properties of firefighting foams with sodium carboxymethyl cellulose and hydrocarbon/silicone surfactants, Chemical Engineering Science 288 (2024) 119733. doi:10.1016/j.ces.2024.119733.

[59] N. Moradpour, J. Yang, P. A. Tsai, Liquid foam: Fundamentals, rheology, and applications of foam displacement in porous structures, Current Opinion in Colloid & Interface Science 74 (2024) 101845. doi:10.1016/j.cocis.2024.101845.

[60] J. Wang, A. V. Nguyen, S. Farrokhpay, A critical review of the growth, drainage and collapse of foams, Advances in Colloid and Interface Science 228 (2016) 55–70. doi:10.1016/j.cis.2015.11.009.

[61] M. J. Shojaei, Y. Méheust, A. Osman, P. Grassia, N. Shokri, Combined effects of nanoparticles and surfactants upon foam stability, Chemical

Engineering Science 238 (2021) 116601. doi:10.1016/j.ces.2021.116601.

[62] Y. Sheng, C. Yan, Y. Li, Y. Peng, L. Ma, Q. Wang, Thermal stability of gel foams stabilized by xanthan gum, silica nanoparticles and surfactants, Gels 7 (4) (2021) 179.

[63] ImageJ. Image Processing and Analysis in Java. URL https://imagej.net/ij/

[64] Y. Sheng, Y. Peng, S. Zhang, Y. Guo, L. Ma, Q. Wang, H. Zhang, Study on thermal stability of gel foam co-stabilized by hydrophilic silica nanoparticles and surfactants, Gels 8 (2) (2022) 123.

[65] A. A. Keller, H. Wang, D. Zhou, H. S. Lenihan, G. Cherr, B. J. Cardinale, R. Miller, Z. Ji, Stability and aggregation of metal oxide nanoparticles in natural aqueous matrices, Environmental science & technology 44 (6) (2010) 1962–1967.

[66] W. Wu, Q. He, C. Jiang, Magnetic iron oxide nanoparticles: synthesis and surface functionalization strategies, Nanoscale research letters 3 (2008) 397–415.

[67] T. S. Horozov, Foams and foam films stabilised by solid particles, Current Opinion in Colloid & Interface Science 13 (2008) 134–140.